*Journal of Zhejiang University-SCIENCE A (Applied Physics & Engineering)* 2025 26(5):407-423
www.jzus.zju.edu.cn; www.springer.com/journal/11582
E-mail: jzus_a@zju.edu.cn

**Research Article**

https://doi.org/10.1631/jzus.A2400134



# Numerical investigation of the transient process of a cover-plate pre-swirl system

Yifu LUO[1,2,3], Qiang DU[1,2,3,4,5,6]✉, Zengyan LIAN[1,2,3], Guang LIU[1,2,3], Lei XIE[1,2,3], Qingzong XU[4]

[1]*Institute of Engineering Thermophysics, Chinese Academy of Sciences, Beijing 100190, China*
[2]*National Key Laboratory of Science and Technology on Advanced Light-duty Gas-turbine, Chinese Academy of Sciences, Beijing 100190, China*
[3]*School of Aeronautics and Astronautics, University of Chinese Academy of Sciences, Beijing 100048, China*
[4]*Qingdao Institute of Aeronautical Technology, Qingdao 266400, China*
[5]*Advanced Gas Turbine Laboratory, Institute of Engineering Thermophysics, Chinese Academy of Sciences, Beijing 100190, China*
[6]*Key Laboratory of Advanced Energy and Power, Chinese Academy of Sciences, Beijing 100190, China*

**Abstract:** A pre-swirl system with a multi-chamber structure is crucial to the secondary air system of an aero engine. The airflow within the pre-swirl system (characterized by high-speed rotation and compressible flow) is complicated. During transient processes in aero engine operation, the pre-swirl system is subjected to upstream fluctuations, which is a less studied aspect. This paper delves into the unsteady flow characteristics within the pre-swirl system. We investigate the influence of different pressure-fluctuation boundary conditions, corresponding to step function, ramp function, and sine function, on the transient response characteristics of the pre-swirl system. The results indicate that the response characteristics are strongly affected by the upstream boundary conditions. An obvious overshoot phenomenon is observed in the actual temperature drop under the step and ramp function conditions. The peak time of the step function is 75% shorter compared to the ramp function. Furthermore, the flow parameters exhibit nonlinear growth during the transient process, emphasizing the need for consideration in future quasi-steady simulations. For the sine function condition, the pressure-fluctuation frequency minimally affects stable values of mass flow rate and actual temperature drop but exerts a substantial influence on the maximum deviation of actual temperature drop of the system. As the frequency increases from 100 Hz to 200 Hz, the maximum deviations for actual temperature drop change from around ±13 K to ±10 K.

**Key words:** Upstream effect; Unsteady flow; Transient response; Cover-plate cavity; Pre-swirl system

## 1 Introduction

In an aero engine, the pre-swirl system plays a crucial role in facilitating the transfer of cooling air from stationary to rotating parts, delivering it to the high-pressure turbine blades at the lowest possible temperature with an appropriate pressure drop. Karabay et al. (1999) proposed categorizing the pre-swirl system into two main types based on the relative positions of the pre-swirl nozzle and receiver hole: the direct-transfer system and the cover-plate system. Fig. 1 shows the schematic diagram of a typical cover-plate pre-swirl system. The pre-swirl system comprises various fluid-flow components, such as cover plates, rotating holes, and labyrinth seals. The cover-plate cavity is employed to discharge cooling air at a convenient radius with subsequent passage to the turbine blades. The nozzles in the pre-swirl system impart a swirling motion to the cooling air in the direction of rotation, accelerating its relative speed. As a result of the work reduction by the turbine disk, the relative total temperature of the air supplied to the blade decreases. The amount of temperature decrease between the stationary pre-swirl nozzle and the rotating receiver holes in a cover plate (fixed to the turbine disk) is determined by the geometrical and operational parameters of the pre-swirl system (Kim et al., 2022).

To the best of our knowledge, Zimmermann (1990) was the first to conduct a computational investigation on a cover-plate pre-swirl system; he improved

✉ Qiang DU, duqiang@iet.cn
Qiang DU, https://orcid.org/0000-0002-8006-3778

Received Mar. 9, 2024; Revision accepted July 25, 2024;
Crosschecked Apr. 7, 2025

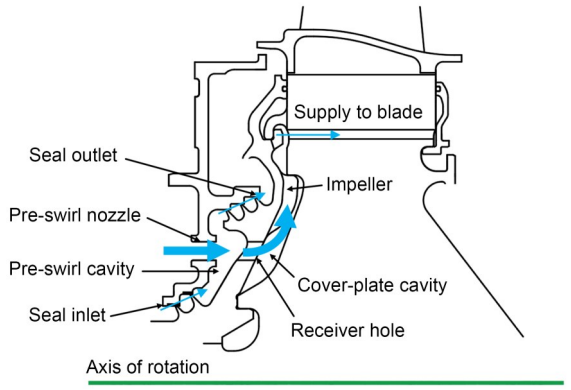


**Fig. 1 Schematic diagram of a typical cover-plate pre-swirl system**

empirical pressure-loss correlations through computational fluid dynamic (CFD) methods. However, his investigation only looked at the area behind the receiver hole. Building upon Zimmermann's work, Popp et al. (1998) used a numerical method to explore a cover-plate system, delving into the physics of the flow in both the pre-swirl cavity and the receiver. Dittmann et al. (2002) experimentally measured the discharge coefficients of receiver holes for the first time, affirming the numerical results reported by Popp et al. (1998). Popp et al. (1998) and Dittmann et al. (2002) both found that the discharge coefficient of the receiver holes was primarily influenced by the relative tangential velocity between the fluid and the turbine disk. Karabay et al. (1999) presented a combined theoretical study with computational and experimental results in an adiabatic cover-plate pre-swirl system. They found that non-dimensional pre-swirl effectiveness depended only on the parameter inlet pre-swirl ratio, and further research (Karabay et al., 2001) suggested that the fluid in the cover-plate cavity would flow radially outward following the principles of free vortex. Other researchers (Liu et al., 2023) were also interested in the effect of geometrical parameters on the flow characteristics of pre-swirl systems. Liao et al. (2014) numerically investigated the effect of geometrical parameters, including the nozzle angle, fillet radius, and ratio of length to diameter of a pre-swirl nozzle. To improve system performance, some novel designs of pre-swirl nozzles and receiver holes were introduced by Liu et al. (2017), Lee et al. (2021), and Gong et al. (2022).

The pre-swirl system faces the issue of unsteady flow, with one issue stemming from the inherent instability of the flow within the pre-swirl system, and another issue resulting from disturbances caused by upstream flow. Under certain geometrical conditions, Dittmann et al. (2002) reported the occurrence of unstable flow in an experimental rig. Ciampoli et al. (2008) used a full unsteady model to capture the unstable flow, revealing that these instabilities were probably attributable to the behavior of the recirculation bubble present in the receiver ducts. Additionally, the pre-swirl system faces other transient issues. When the state of an aero engine changes, the internal flow in the second air system undergoes a complex transient process. Nicholas et al. (2023) showed that the tip-clearance growth varied throughout a typical transient cycle, resulting in inlet distortion for a downstream pre-swirl system. The filling and discharge of gas in the vessels (Dutton and Coverdill, 1997; Zhang and Naguib, 2011), the inherent inertial effects in the flow, and mechanical rotation processes (Gallar et al., 2011; Lin et al., 2022) affect the dynamic response of the system during transitions. The strong non-linear characteristics typically result in peak loads for an aero engine during the transient process. The risk of aero engine disks during these transitions can be several times greater than that experienced under steady-state conditions (Ding et al., 2018). To simulate the transient process, Benim et al. (2004) proposed guidelines for a pre-swirl system based on the quasi-steady model. However, Nikolaidis et al. (2020) pointed out that under extreme operating conditions, transient effects must be considered, as several phenomena may occur that cannot be captured by steady or quasi-steady simulation. Moreover, Gan et al. (2024) emphasized that during the transient process, the time resolution is indispensable for the safety evaluation of complex aero engine systems.

The literature review reveals a gap in discussions regarding the complex dynamic characteristics of cover-plate pre-swirl systems during the transient process. This study addresses the gap by using 3D full unsteady numerical simulations to investigate the flow characteristics of a cover-plate pre-swirl system during the transient process. Based on actual aero engine designs and previous studies (Liu et al., 2018, 2021), we designed a simplified structure for the cover-plate pre-swirl system, consisting of five main components: the inlet chamber, pre-swirl nozzle, pre-swirl cavity, receiver hole, and cover-plate cavity (or rotor-rotor cavity). To account for the mixing effect in the pre-swirl cavity downstream from the nozzles, a seal structure was

included. The primary objective of this research was to evaluate the effects of different upstream inlet conditions on the temperature drop and transient response of the cover-plate pre-swirl system, providing valuable insights for optimizing aero engine designs.

## 2 Models and numerical approach

### 2.1 Governing equations

The 3D unsteady-state compressible Reynolds-averaged Navier-Stokes equations, coupled with the shear stress transport (SST) $k$-$\omega$ turbulence model (Menter, 1994), were adopted as the governing equations.

#### 2.1.1 Governing equations of the stationary subdomain

The calculation domain in this study is divided into two subdomains: the stationary subdomain and rotating subdomain. The governing equations in the stationary subdomain are as follows:

(1) Mean mass conservation:

$$\frac{\partial \rho}{\partial t}+\frac{\partial(\overline{\rho \boldsymbol{v}_i})}{\partial \boldsymbol{x}_i}=0, \tag{1}$$

where $\rho$ is the density, $t$ is the time, $\boldsymbol{v}$ is the velocity, $\boldsymbol{x}$ is the Cartesian coordinate, the superscript '–' is used to denote the ensemble average, and the subscript $i$ is the Einstein notation.

(2) Reynolds-averaged momentum conservation:

$$\frac{\partial(\overline{\rho \boldsymbol{v}_i})}{\partial \boldsymbol{x}_i}+\frac{\partial(\overline{\rho \boldsymbol{v}_j \boldsymbol{v}_i})}{\partial \boldsymbol{x}_j}=-\frac{\partial(\overline{p})}{\partial \boldsymbol{x}_i}+\frac{\partial \hat{\boldsymbol{\tau}}_{ij}}{\partial \boldsymbol{x}_j}, \tag{2}$$

where $p$ is the pressure, and $\hat{\boldsymbol{\tau}}_{ij}$ is the total viscous stress tensor.

(3) Mean energy conservation:

$$\frac{\partial(\rho E)}{\partial t}+\frac{\partial(\overline{\rho \boldsymbol{v}_j} H)}{\partial \boldsymbol{x}_j}=\frac{\partial}{\partial \boldsymbol{x}_j}\left[\overline{\boldsymbol{v}}_i \hat{\boldsymbol{\tau}}_{ij}+(\mu+\sigma_k \mu_t)\frac{\partial k}{\partial \boldsymbol{x}_j}-\boldsymbol{q}_j\right], \tag{3}$$

where $E$ is the total energy, $H$ is the total enthalpy, $k$ is the turbulent kinetic energy, $\sigma_k$ is the closure coefficient, $\mu$ is the molecular dynamic viscosity, and $\mu_t$ is the turbulent eddy viscosity coefficient. The total viscous stress tensor $\hat{\boldsymbol{\tau}}_{ij}$ is given by:

$$\hat{\boldsymbol{\tau}}_{ij}=2\mu\left[\left(\frac{\partial \overline{\boldsymbol{v}}_i}{\partial \boldsymbol{x}_j}+\frac{\partial \overline{\boldsymbol{v}}_j}{\partial \boldsymbol{x}_i}\right)-\frac{1}{3}\left(\frac{\partial \overline{\boldsymbol{v}}_k}{\partial \boldsymbol{x}_k}\right)\boldsymbol{\delta}_{ij}\right]-\rho\,\overline{\boldsymbol{v}_i' \boldsymbol{v}_j'}, \tag{4}$$

where $\boldsymbol{\delta}_{ij}$ is the Kronecker delta. The symbol '′' is used to denote the fluctuation with respect to the ensemble average. The heat flux vector $\boldsymbol{q}_j$ is given by:

$$\boldsymbol{q}_j=-\left(\frac{\mu}{Pr_L}+\frac{\mu_t}{Pr_T}\right)\frac{\partial h}{\partial \boldsymbol{x}_j}, \tag{5}$$

where $Pr_L$ and $Pr_T$ are the laminar and turbulent Prandtl numbers, respectively, and $h$ is the enthalpy. For the ideal gas, $h=C_pT$, where $C_p$ is the specific heat capacity under a constant pressure, and $T$ is the temperature. We will choose the working fluid as the air-ideal gas, with a specific heat capacity $C_p$ set to 1004.4 J/(kg·K).

In Eq. (4), $-\rho\,\overline{\boldsymbol{v}_i' \boldsymbol{v}_j'}$ is the Reynolds stress, which is an unknown quantity, representing the energy transfer caused by turbulent fluctuations. The Boussinesq approximation is invoked to relate the Reynolds stress to the mean strain rate, and thus:

$$-\rho\,\overline{\boldsymbol{v}_i' \boldsymbol{v}_j'}=\mu_t\left(\frac{\partial \boldsymbol{v}_i}{\partial \boldsymbol{x}_j}+\frac{\partial \boldsymbol{v}_j}{\partial \boldsymbol{x}_i}\right)-\frac{2}{3}\left(\rho k+\mu_t\frac{\partial \boldsymbol{v}_k}{\partial \boldsymbol{x}_k}\right)\boldsymbol{\delta}_{ij}. \tag{6}$$

The coupling of turbulence models with the Navier-Stokes equations involves specific relationships that relate the $\mu_t$ with the time-averaged quantities. In the SST turbulence model (Menter, 1994), $\mu_t$ is defined as:

$$\mu_t=\frac{\rho a_1 k}{\max(a_1\omega,\ \Omega_a F_2)}, \tag{7}$$

where $a_1$ is a constant, $\omega$ is the eddy dissipation rate, $\Omega_a$ is the absolute value of the vorticity, and $F_2$ is a function with a value of one for boundary-layer flows and zero for free shear layers. The turbulent kinetic energy $k$ transport equation is:

$$\frac{\partial}{\partial t}(\rho k)+\frac{\partial}{\partial \boldsymbol{x}_j}(\rho k \boldsymbol{v}_j)=\boldsymbol{\tau}_{ij}\frac{\partial \boldsymbol{v}_i}{\partial \boldsymbol{x}_j}+\frac{\partial}{\partial \boldsymbol{x}_j}\left[(\mu+\sigma_k\mu_t)\frac{\partial k}{\partial \boldsymbol{x}_j}\right]-\beta^*\rho k\omega, \tag{8}$$

$$\boldsymbol{\tau}_{ij}=\mu_t\left(\frac{\partial \boldsymbol{v}_i}{\partial \boldsymbol{x}_j}+\frac{\partial \boldsymbol{v}_j}{\partial \boldsymbol{x}_i}-\frac{2}{3}\frac{\partial \boldsymbol{v}_k}{\partial \boldsymbol{x}_k}\boldsymbol{\delta}_{ij}\right)-\frac{2}{3}\rho k\boldsymbol{\delta}_{ij}, \tag{9}$$

and the eddy dissipation rate $\omega$ transport equation is:

$$\frac{\partial}{\partial t}(\rho\omega)+\frac{\partial}{\partial \boldsymbol{x}_j}(\rho\omega \boldsymbol{v}_j)=\frac{\gamma\omega}{k}\boldsymbol{\tau}_{ij}\frac{\partial \boldsymbol{v}_i}{\partial \boldsymbol{x}_j}-\beta_1\rho\omega^2+\frac{\partial}{\partial \boldsymbol{x}_j}\left[(\mu+\sigma_\omega\mu_t)\frac{\partial\omega}{\partial \boldsymbol{x}_j}\right]+2(1-F_1)\rho\sigma_{\omega2}\frac{1}{\omega}\frac{\partial k}{\partial \boldsymbol{x}_j}\frac{\partial\omega}{\partial \boldsymbol{x}_j}, \tag{10}$$

where $F_1$ is a blending function, which is designed to have a value of one in the sublayer and logarithmic region of the boundary layer and to gradually change to zero in the wake region. $\beta_1$, $\beta^*$, $\sigma_k$, $\sigma_\omega$, $\sigma_{\omega2}$, and $\gamma$ are several closure coefficients, the values of which can be found elsewhere (Wilcox, 1988; Menter, 1994). To solve Eqs. (1)–(3), (8), and (9), it is necessary to include the gas state equation for the ideal gas:

$$p=\rho RT, \tag{11}$$

where $R$ is the molar gas constant.

#### 2.1.2 Governing equations of the rotating subdomain

The governing equations of fluid flow for a steadily rotating frame are similar to Eqs. (1)–(3), except that they use $\boldsymbol{v}=\boldsymbol{v}_r+\boldsymbol{u}_r$, where $\boldsymbol{v}$ is the absolute velocity, $\boldsymbol{v}_r$ is the relative velocity, $\boldsymbol{u}_r=\boldsymbol{\omega}_a\times\boldsymbol{r}$ is the velocity of the rotating frame relative to the inertial reference frame, $\boldsymbol{\omega}_a$ is the angular velocity of the rotating frame, and $\boldsymbol{r}$ is the spatial coordinate vector.

#### 2.1.3 Interface treatment approach

The interface is applied between different subdomains, using the general grid interface (GGI) method. In the commercial code Ansys CFX, there are three different options for the interface treatment between stationary and rotating subdomains. In this study, we opted for a slide-plane interface, employing a full transient simulation that incorporated a rotational shift between stationary and rotating meshes at every time step. The mass, momentum, and energy flux were conserved on the interface. This facilitated the capture of an unsteady flow structure within the flow field, arising from the varying relative positions of the pre-swirl nozzle and the receiver hole (Karnahl et al., 2012).

### 2.2 Numerical models

The model studied in this paper was simplified according to the real engine pre-swirl system, as illustrated in Fig. 2. The pre-swirl system included three chambers: the inlet chamber, the pre-swirl cavity, and the cover-plate cavity. The pre-swirl system was classified into two subdomains based on motion: stationary and rotating. There were a total of 11 nozzles, 33 receiver holes, and 33 supply holes in the system. The pre-swirl nozzles were located at a low radius in the stationary subdomain, with a pre-swirl angle of $\alpha$ and nozzle diameter of $D_{nozzle}$. To save computational resources, we chose 1/11 of the entire pre-swirl system as a computational domain for simulation. The 2D section for the computational model is shown in Fig. 2b. The

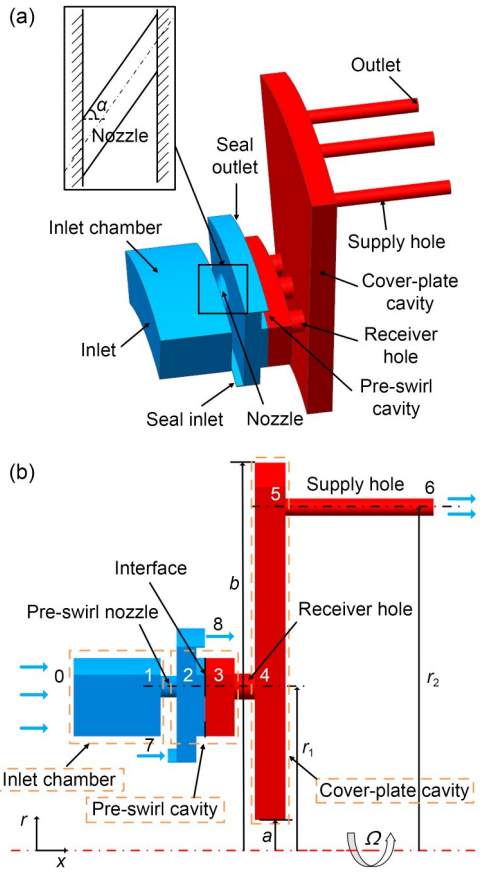


**Fig. 2 Cover-plate pre-swirl cooling system: (a) 3D computational domain (the stationary subdomain is blue and the rotating subdomain is red); (b) 2D section. Stations 0–8 are labelled on this diagram, where 0 refers to conditions at the inlet of the inlet chamber, 1 refers to conditions upstream of the pre-swirl nozzle, 2 refers to conditions downstream of the pre-swirl nozzle, 3 refers to conditions at the receiver-hole inlet, 4 refers to conditions at the receiver-hole outlet, 5 refers to conditions at the supply-hole inlet, 6 refers to conditions at the supply-hole outlet, 7 refers to conditions at the seal inlet, and 8 refers to conditions at the seal outlet. References to color refer to the online version of this figure**

inlet (0) and outlet (6) radii of the pre-swirl system are $r_1$ and $r_2$, respectively. The cover-plate cavity had an inner radius of $a$ and an outer radius of $b$. Other detailed parameters are given in Table 1.

**Table 1 Pre-swirl system parameters**

| Parameter | Value |
|---|---|
| Height of inlet 7 (mm) | 0.12 |
| Height of outlet 8 (mm) | 0.16 |
| Inner radius, $a$ (mm) | 30.9 |
| Nozzle diameter, $D_{nozzle}$ (mm) | 2.5 |
| Outer radius, $b$ (mm) | 70.8 |
| Pre-swirl angle of nozzle, $\alpha$ (°) | 70 |
| Receiver-hole diameter (mm) | 3 |
| Radius of inlet 0, $r_1$ (mm) | 45 |
| Radius of outlet 6, $r_2$ (mm) | 65.6 |
| Supple hole diameter (mm) | 2 |
| Rotating velocity, $\Omega$ (r/min) | 45000 |

Ansys ICEM CFD was used for mesh formation and unstructured grids were used to divide the computational domains. As shown in Fig. 3, the $y^+$ was set to around 1–3 in most areas of the cover-plate cavity. The multi-layer hexahedral mesh was used on the solid surface. The height of the first layer of the grid near the wall was set to 0.001 mm. The height ratio was set to 1.2 and the total number of layers was set to 20 to ensure a natural transition from boundary-layer grid to central grid. To check the mesh sensitivity, we carried out a mesh independence study. Three different mesh levels were studied, including 3.95 million, 5.61 million, and 8.55 million cells, corresponding to coarse mesh, medium mesh, and fine mesh, respectively. The Richardson-extrapolated solution (subscript RE) can be expressed as (Roache, 1998; Bonfiglioli and Paciorri, 2014):

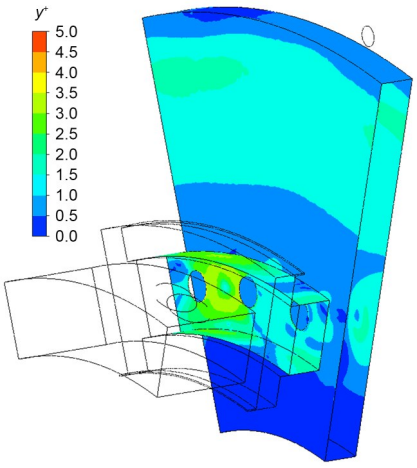


**Fig. 3 Distribution of $y^+$ in the rotating subdomain**

$$f_{RE}=\frac{f_2^2-f_1f_3}{2f_2-f_3-f_1}, \tag{12}$$

where the subscripts from 1 to 3 indicate increasing resolution from coarse to fine mesh. Considering $f$ as the value of average pressure in cover-plate cavity $f=p_{ave}$, the error with respect to the Richardson-extrapolated solution is:

$$\varepsilon_{RE}=\frac{|f-f_{RE}|}{f_{RE}}. \tag{13}$$

The convergence of error (Roy et al., 2003; Thomas et al., 2008) was studied and is shown in Fig. 4. As the grid became finer, the error decreased and achieved 4th-order convergence. The mesh including 5.61 million cells is employed in the following computation because the error is less than $10^{-3}$.

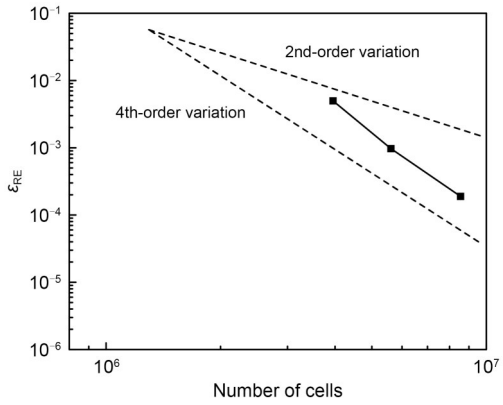


**Fig. 4 Results of mesh independence validation**

## 2.3 Solver setup and computational boundary conditions

Based on the finite volume method, we solved the unsteady 3D Reynolds-averaged Navier-Stokes equations with the SST $k$-$\omega$ turbulence model. All solid walls were set to the adiabatic boundary condition. Fluid was set to be air-ideal gas. The total pressure, total temperature, and turbulence intensity were set at inlet 0 (shown in Fig. 2b). Mass flow rate, turbulence intensity, and total temperature were set at the seal inlet. Static pressure was set for both the seal outlet and

supply-hole outlet. Detailed boundary conditions are shown in Table 2. The steady simulation results were utilized as the initial value for the transient simulation. In unsteady simulation, the advection scheme was set to a high resolution. We employed the second-order backward Euler time discretization as the transient scheme. The convergence criteria of the normalized root mean square (RMS) of residuals were less than $10^{-4}$. Coefficient loops were set within a range from 1 to 10. As shown in Table 3, four different intake functions were set at surface inlet 0 (shown in Fig. 2b) using CFX expression language (CEL). The step function and ramp function corresponded to the strong transient process and weak transient process, respectively. Sine function types I and II were put in place to study the effect of inlet fluctuation frequency on the pre-swirl system. In the transient process simulation, we used unsteady simulation results as the initial values; the convergence criteria were the same as those used in the unsteady simulation. This design permitted us to investigate the effects of different intake functions on the pre-swirl system. All the CFD simulations were done with the commercial code CFX 21.0.

**Table 2 Detailed boundary conditions**

| Parameter | Description |
|---|---|
| Inlet total pressure | Defined by function |
| Inlet total temperature (K) | 653 |
| Static pressure at supply-hole outlet (kPa) | 567 |
| Mass flow rate at seal inlet (whole ring) (kg/s) | 0.0149 |
| Total temperature at seal inlet (K) | 638 |
| Static pressure at seal outlet (kPa) | 566 |
| Rotating velocity (r/min) | 45000 |

**Table 3 Intake function**

| Function | Expression |
|---|---|
| Case I: step function | $p^*_{\text{in},0}=\begin{cases}1178, & t=0\text{ s},\\ 1178+\Delta p, & t>0\text{ s},\end{cases}$ where $\Delta p$=117.8 kPa |
| Case II: ramp function | $p^*_{\text{in},0}=\begin{cases}1178, & t=0\text{ s},\\ 1178+k_s t, & 0\text{ s}<t\leqslant 0.01\text{ s},\end{cases}$ where slope $k_s$=11780 kPa/s |
| Case III: sine function, type I | $p^*_{\text{in},0}=\begin{cases}1178, & t=0\text{ s},\\ 1178+117.8\sin(200\pi t), & t>0\text{ s}\end{cases}$ |
| Case IV: sine function, type II | $p^*_{\text{in},0}=\begin{cases}1178, & t=0\text{ s},\\ 1178+117.8\sin(400\pi t), & t>0\text{ s}\end{cases}$ |

$p^*_{\text{in},0}$ is the inlet total pressure (kPa)

## 2.4 Numerical approach validation

To further verify the accuracy of the calculation method, we conducted a comparative study with experimental data from a radial outflow cover-plate cavity (Owen et al., 1985). As shown in Figs. 5 and 6, this rig had 32 radial outflow holes. The angular spacing of the holes was 11.25° and the hole size was 32 mm in diameter. The gas flowed into the cavity at the axial inlet and then flowed out from radial outflow holes. Fig. 5 shows the calculation domain and grid division. Structured hexahedral grid generation was used in all spaces. The simulation results with the SST $k$-$\omega$ turbulence model are shown in Fig. 6, illustrating the distribution of the swirl ratio $\beta$ and volume flow-rate coefficient $C_W$. The swirl-ratio distribution at mid-cavity closely matched the experimental data both qualitatively and quantitatively. Therefore, we believe that the SST $k$-$\omega$ turbulence model could provide accurate calculation results for subsequent studies.

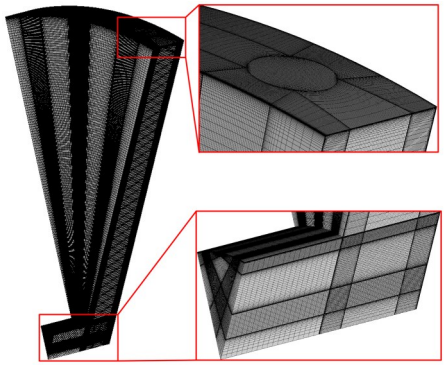

**Fig. 5 Grid distribution for the experimental validation model**

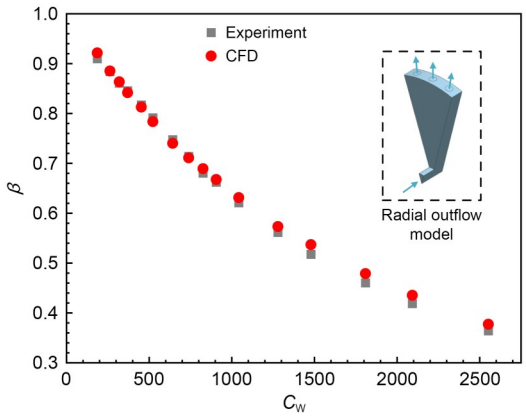


**Fig. 6 Comparison of swirl ratio $\beta$ between numerical prediction and experimental result (Owen et al., 1985) for the radial outflow model**

Explicit and implicit are common terms used to describe numerical solution schemes. An explicit computation means that the dependent variables can be directly calculated using known quantities. On the other hand, an implicit approach is employed when the dependent variables are determined by interconnected sets of equations, requiring either a matrix or iterative technique to achieve the solution. Each explicit time-stepping scheme remains stable only up to a certain value of the time step d$t$ due to constraints imposed by the Courant-Friedrichs-Lewy (CFL) condition (Courant et al., 1928; Blazek, 2015). However, in CFX an implicit time-stepping scheme is used, which means the CFL condition does not apply. To precisely predict the transient process of a pre-swirl system, the selected time step should be small enough to accurately capture the relevant time scale. We tested three different time steps, corresponding to 16, 32, and 48 steps per period, i.e., 2.04°, 1.02°, and 0.68° per time step. As shown in Fig. 7, pressure distribution $p/p^*_{\text{in},0}$ in the cover-plate cavity showed that 32 time steps (corresponding to time step d$t$=3.79×10$^{-6}$ s) provided a sufficiently accurate solution.

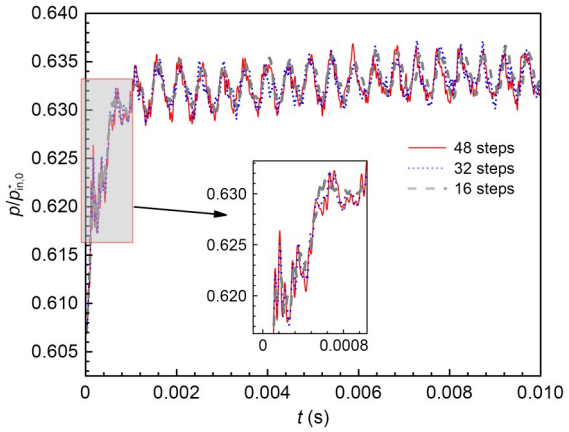


**Fig. 7 Results of time-step independence analysis**

## 3 Parameter definition and theoretical analysis

Due to factors such as the bulk-cavity effect, rotation effect, and air compressibility, the change in airflow parameters at each position of the pre-swirl system flow path was delayed to varying degrees when an upstream airflow disturbance occurred. In order to facilitate quantitative analysis of the response speed of each parameter in the response process, several transient response evaluation parameters are introduced here (Table 4).

**Table 4 Transient response parameters**

| Parameter | Definition |
|---|---|
| Response time, $t_r$ | The shortest time required for the flow parameters to reach the stable value |
| Peak time, $t_p$ | The time required for the flow parameters to reach the maximum or minimum |
| Maximum deviation, $h(t_p)$ | The maximum (minimum) value of the flow parameters in the transient response process |
| Overshoot amount, $\sigma$ | $\sigma=\lvert h(t_p)-h(\infty)\rvert/h(\infty)\times100\%$, where $h(\infty)$ is the stable value of flow parameters |
| Dimensionless jump amplitude, $I$ | $I=h(\infty)/h_0\times100\%$, where $h_0$ is the initial value of flow parameters |

We have defined some other parameters to aid in the subsequent analysis of results.

(1) Retention mass flow $\Delta m$:

$$\Delta m = m_0 + m_7 - m_6 - m_8, \tag{14}$$

where $m_0$, $m_7$, $m_6$, or $m_8$ represents a transient total mass flow rate at surface 0, 7, 6, or 8 (Fig. 2), respectively, and $\Delta m$ denotes the mass of gas trapped in the pre-swirl system per unit time.

(2) Swirl ratio $\beta$:

$$\beta = \frac{V_\phi}{\omega_a r}, \tag{15}$$

where $V_\phi$ is the absolute tangential velocity, $\omega_a$ is the angular velocity, and $r$ is the local radius.

(3) Relative total temperature $T^*_{\text{rel}}$:

$$T^*_{\text{rel}} = T + \frac{V_A^2}{2C_p} + \frac{V_R^2}{2C_p} + \frac{(V_\phi - \omega_a r)^2}{2C_p}, \tag{16}$$

where $V_A$ is the axial velocity, and $V_R$ is the radial velocity. The relationship between the relative total temperature and absolute total temperature $T^*$ is:

$$T^*_{\text{rel}} = T^* + \frac{(\omega_a r)^2}{2C_p} - \frac{V_\phi \omega_a r}{C_p}, \tag{17}$$

and $\Delta T_{\text{sys}}$ is the actual temperature drop of the system:

$$\Delta T_{\mathrm{sys}} = T_0^* - T_{6,\,\mathrm{rel}}^* = \frac{2V_\phi \omega_a r - (\omega_a r)^2}{2C_p}, \qquad (18)$$

which is defined as the difference between the total temperature of the pre-swirl system inlet ($T_0^*$) and the relative total temperature of the pre-swirl system outlet ($T_{6,\,\mathrm{rel}}^*$).

## 4 Results and discussion

### 4.1 Case I (extreme operating conditions) and Case II (normal operating conditions)

These two sets of conditions are differentiated by the inlet pressure. Case I simulates the flow when there is a step-change in the pre-swirl inlet conditions. The pre-swirl system first operates in a state of equilibrium, and then the boundary condition suddenly changes to its maximum values. Case II simulates pre-swirl operation when there is a smooth change in the boundary condition. The initial values of the pre-swirl system operating conditions are the same as in Case I (shown in Table 3). The variation in the inlet boundary condition represents the transient performance of the secondary air system during acceleration, with the inlet pressure varying linearly from the initial to the final value.

Fig. 8 shows the transient response of the mass flow parameters with step and ramp functions. At outlet 6 of the supply hole (shown in Fig. 8a), the mass flow rate increased rapidly at first and then slowly increased to a stable value. For step and ramp functions, the stable values were consistent, which is related to the pressure-jump amplitude. When the inlet pressure jumped by 10%, the dimensionless jump amplitude $I$ was around 110% for the supply-hole outlet and seal outlet (shown in Fig. 8b). However, it is clear from Fig. 8a that the duration of the fast-increase period was much longer for the ramp function than for the step function. This difference arose because a step function induces an immediate and abrupt pressure change, leading to a quick adjustment in flow rate. In contrast, a ramp function introduces the pressure change gradually, resulting in a prolonged transition period as the system continuously adjusts to the changing conditions. At seal outlet 8 (shown in Fig. 8b), the change in mass flow rate was similar to that at the outlet of the supply hole. When the mass flow rate reached a stable value, the fluctuation was more intense. From

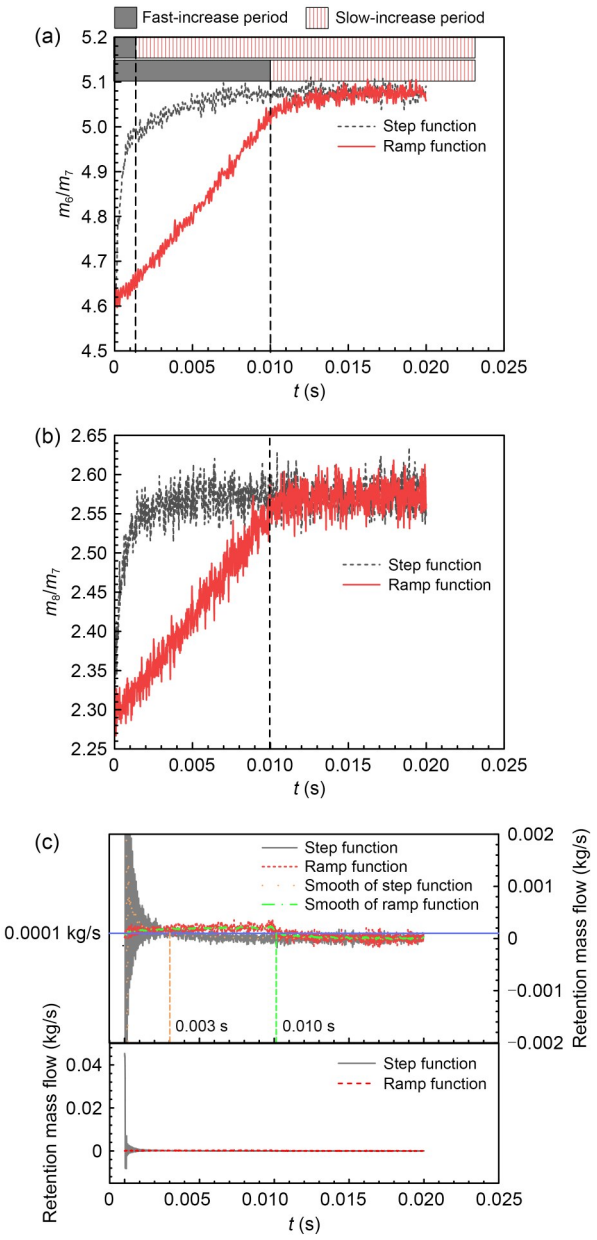


**Fig. 8 Transient response of mass flow parameters of the pre-swirl system with step and ramp functions: (a) response of mass flow rate at outlet of the supply hole; (b) response of mass flow rate at the seal outlet; (c) response of retention mass flow for the pre-swirl system (the upper part is a localized magnified view)**

$t$=0 s to $t$=0.02 s, the increase in mass flow (whether at the outlet of the supply hole or at the seal outlet) exhibited definite nonlinearity. Therefore, using the quasi-steady state simulation for the transient process meant that we also needed to consider the nonlinear factors, including pressure and mass flow. Fig. 8c shows how we used retention mass flow $\Delta m$ to determine

flow fluctuation in the pre-swirl system. We noticed that the $\Delta m$ oscillation decreased to 0 kg/s, as shown in the lower part of Fig. 8c. In the upper part of Fig. 8c, a localized magnified view is shown. It can be seen that whether with a step function or a ramp function, the retention mass flow $\Delta m$ first increased and then decreased to 0 kg/s. Defining the response time $t_r$ was challenging for retention mass flow $\Delta m$. We believe that when the smoothed mass flow curve begins to decline and its value is less than 0.0001 kg/s, the retention mass flow $\Delta m$ has reached a stable state. Thus, the response times corresponding to the step function and the ramp function are 0.003 s and 0.010 s, respectively. Figs. 9 and 10 show the volume-average parameter response in the cover-plate cavity. For the step and ramp functions, the volume-average density $\rho_{ave}$ increased at first and then rose to a stable value around $\rho_{ave}$=3.88 kg/m$^3$. The dimensionless jump amplitude $I$ of $\rho_{ave}$ for both inlet functions was calculated as 4.21%. For both functions, the volume-average density $\rho_{ave}$ first increased rapidly and then slowly rose to a stable value. When $t$>0.16 s, the values of the two curves were essentially equal. In Fig. 10, the curves of volume-average relative total pressure $p^*_{rel}$ follow a similar pattern, which increases at first and then rises to a stable value around $p^*_{rel}$=721 kPa. When $t$<0.0012 s, the volume-average relative total pressure growth rate for the step function was much larger than for the ramp function. When $t$>0.01 s, $p^*_{rel}$ values for both inlet functions were almost the same. The dimensionless jump amplitude $I$ of $p^*_{rel}$ for both inlet functions was $I$=3.77%.

Fig. 11 shows the actual temperature drop $\Delta T_{sys}$ for the pre-swirl system response. In contrast to the response of the volume-average parameters, the $\Delta T_{sys}$ response exhibited a noticeable overshoot phenomenon. For both step and ramp functions, $\Delta T_{sys}$ initially decreased to a maximum deviation $h(t_p)$ and then gradually increased up to a stable value, settling around $\Delta T_{sys}$=2.5 K. From Eq. (18), it is evident that the actual temperature drop $\Delta T_{sys}$ depends on the pre-swirl inlet total temperature $T^*_0$ and the outlet relative total temperature $T^*_{6,\,rel}$. In this study, $T^*_0$ is given by boundary conditions as 653 K. Therefore, $\Delta T_{sys}$ is only affected by changes in the $T^*_{6,\,rel}$. This pattern of $\Delta T_{sys}$ change can be explained from the perspective of retention mass flow. From Fig. 8c, it can be seen that in the early stage of the transient process, the inlet mass flow rate of the pre-swirl is always greater than the outlet flow rate, causing most of the incoming airflow to be retained inside the cover-plate cavity. Due to compression effects, this portion of the fluid has higher pressure and affects the downstream fluid, resulting in an increase

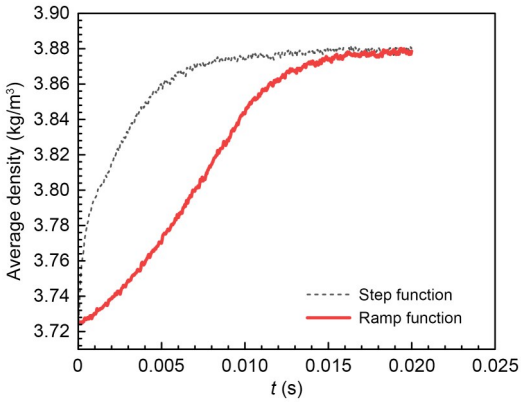


**Fig. 9 Volume-average density in the cover-plate cavity response**

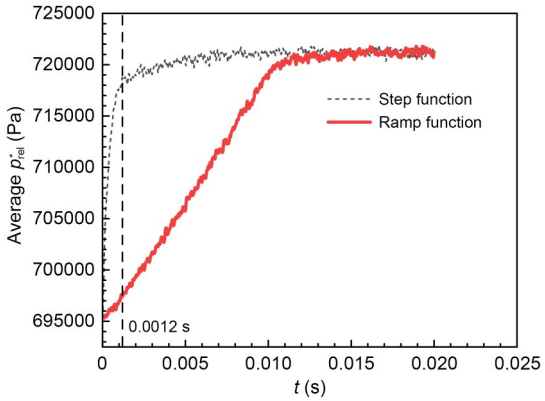


**Fig. 10 Volume-average relative total pressure in the cover-plate cavity response**

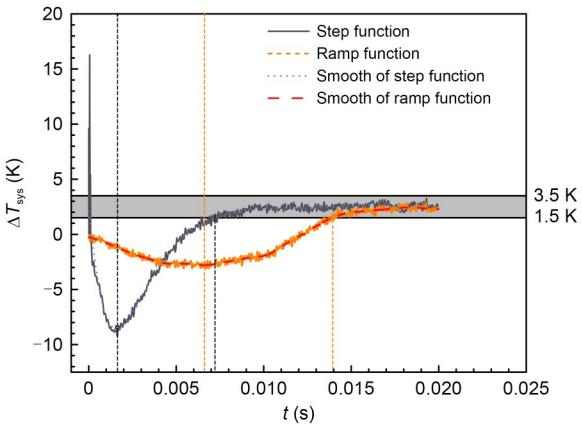


**Fig. 11 Actual temperature-drop response for the pre-swirl system**

in the downstream fluid's internal energy, which in turn increases the relative temperature $T^*_{6,\,\mathrm{rel}}$. In the later stage of the transient process, the flow field gradually stabilizes and the retention mass flow gradually decreases to zero. The work capability of the retention mass flow downstream diminishes, and the relative total temperature $T^*_{6,\mathrm{rel}}$ also decreases to a stable value. We found that the peak time $t_\mathrm{p}$ of the step function, which was 0.00165 s, was 75% shorter compared to that of the ramp function (0.00662 s). In addition, the maximum deviation $h(t_\mathrm{p})$ for the step function was smaller than that for the ramp function. For the step function, the maximum deviation $h(t_\mathrm{p})$ was around −9 K, corresponding to an overshoot amount $\sigma$=460%. For the ramp function, the maximum deviation $h(t_\mathrm{p})$ was around −3 K, corresponding to an overshoot amount $\sigma$=220%. In the secondary air system of aircraft engines, the $\Delta T_{\mathrm{sys}}$ overshoot phenomenon indicates a decrease in the quality of air supply, which can increase the risk of turbine-blade erosion. From Fig. 11, it can also be seen that the final $\Delta T_{\mathrm{sys}}$ fluctuated around 2.5 K. We define the $\Delta T_{\mathrm{sys}}$ as stable when its fluctuation range is within (2.5±1.0) K, corresponding to the black shaded area in Fig. 11. The response time is the time from the initial moment until $\Delta T_{\mathrm{sys}}$ enters the stable range. We can conclude that the step-function entrance has a shorter response time $t_\mathrm{r}$ than the ramp-function entrance. For the step function, the response time $t_\mathrm{r}$ was around 0.0072 s, while for the ramp function, it was around 0.0140 s.

The response of parameters at different points in the pre-swirl system is shown in Fig. 12. We chose points in the inlet chamber (inlet 0 shown in Fig. 2b) and supply-hole inlet (inlet 5 shown in Fig. 2b). Figs. 12a, 12b, and 12c show how the density $\rho$, pressure $p$, and temperature $T$ were normalized by the average values obtained during the transition process, respectively. With the step function, the parameters at inlet 0 exhibited a linear distribution after perturbation at the initial time. In the case of the ramp function, the density and pressure parameters at inlet 0 displayed a linear distribution after slope growth at 0 s<$t$<0.01 s. The response of parameters at the downstream point (inlet 5) differed significantly. The oscillatory rise of density

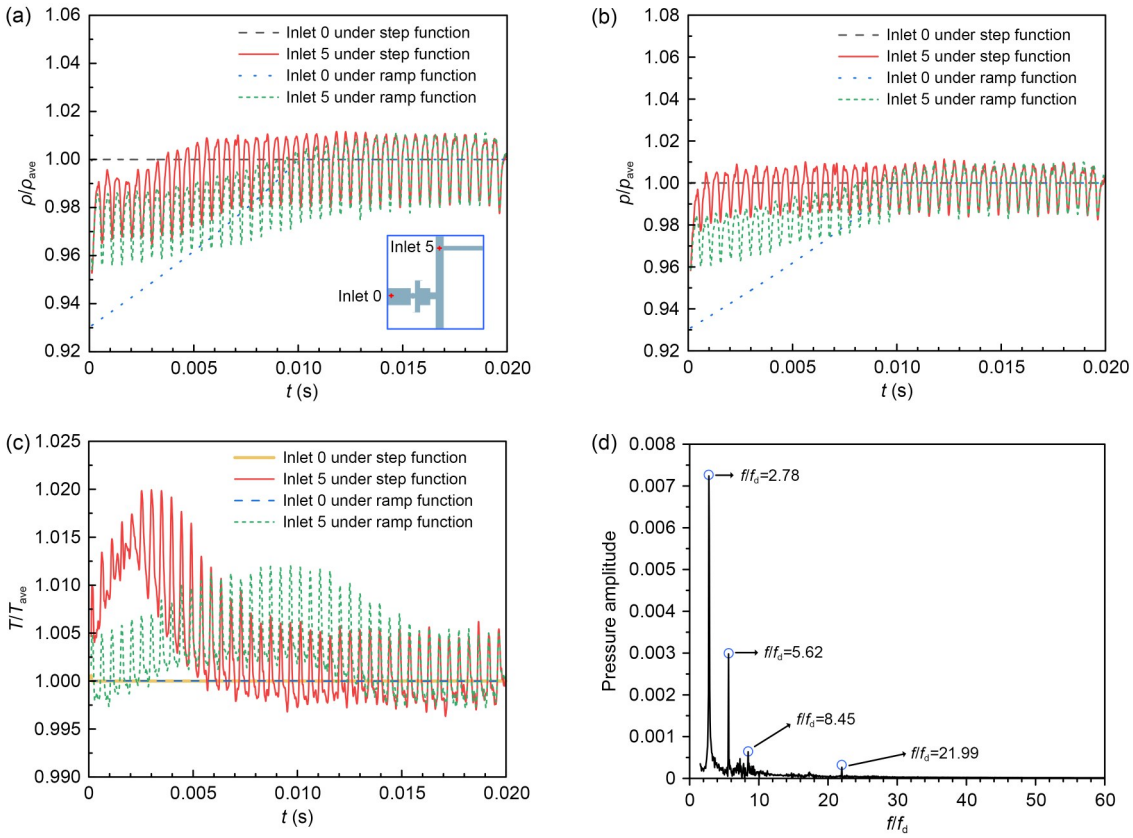


**Fig. 12 Normalized parameter response at different points in the pre-swirl system: (a) density response; (b) pressure response; (c) temperature response; (d) pressure–frequency spectra at inlet 5 with the step function**

and pressure parameters at inlet 5 was notable. The step disturbance was transmitted downstream faster, causing the downstream parameters to reach a stable value more quickly. With regard to temperature, the parameter at inlet 5 initially rose and then fell to a stable value. We attribute the temperature overshoot phenomenon to the low thermal diffusivity of air. In Fig. 12d, we present the frequency spectra obtained from the Fourier transform of the pressure at inlet 5 with the step function. The frequency was normalized with respect to the rotational frequency of the cover-plate cavity ($f_d$). As the monitor points were fixed in the cover-plate cavity, the frequency spectra illustrate the relative movement of flow structures. A dominant frequency $f/f_d$= 2.78 and its double and triple frequencies were detected. As inlet 5 was closed to the cover-plate cavity shroud, it is reasonable to assume that the dominant peak corresponds to the rotational frequency of the vortex structures due to the shroud. This assumption could explain the distributions near the shroud in Fig. 15, which illustrates how circumferential pressure and streamline distribution varied with time. However, due to the limitations of the simulation method we used, achieving a more accurate vortex structure in future studies would require high-precision simulation.

In order to further explain the flow characteristics in the cover-plate cavity during the transient process, we illustrate in Fig. 13 the pressure distribution at different times on the mid-section plane of the cover-plate cavity. We selected five moments, corresponding to $t_1$= $2.65\times10^{-5}$ s, $t_2$=$2.39\times10^{-4}$ s, $t_3$=$4.51\times10^{-4}$ s, $t_4$=$6.63\times10^{-4}$ s, and $t_5$=$8.75\times10^{-4}$ s, to investigate pressure-distribution fluctuation during the transition process. Due to the effect of centrifugal pressurization, static pressure gradually increased during the radial outflow process. At each time step, the circumferential static pressure distribution at a high radius was uneven, which was influenced by rotation. As time progressed, the static pressure distribution in the cover-plate cavity increased overall, driven by the upstream pressure transition. For both step-function and ramp-function intakes, the static pressure distribution at different times exhibits similarities. In the low-radius region, various scale vortex structures emerged in the flow field due to gas disturbance after passing the receiver holes. In the high-radius region, gas entrainment by the cavity resulted in predominantly circumferential velocity.

Fig. 14 illustrates the instantaneous swirl-ratio distribution in the receiver hole at the same time shown in Fig. 13. In the pre-swirl cavity, the swirl-ratio distribution was uneven. Behind the pre-swirl nozzle, the swirl ratio was around 1.6, forming a region with a large swirl ratio, while the swirl ratios on both sides were relatively low due to the ejection action. As time

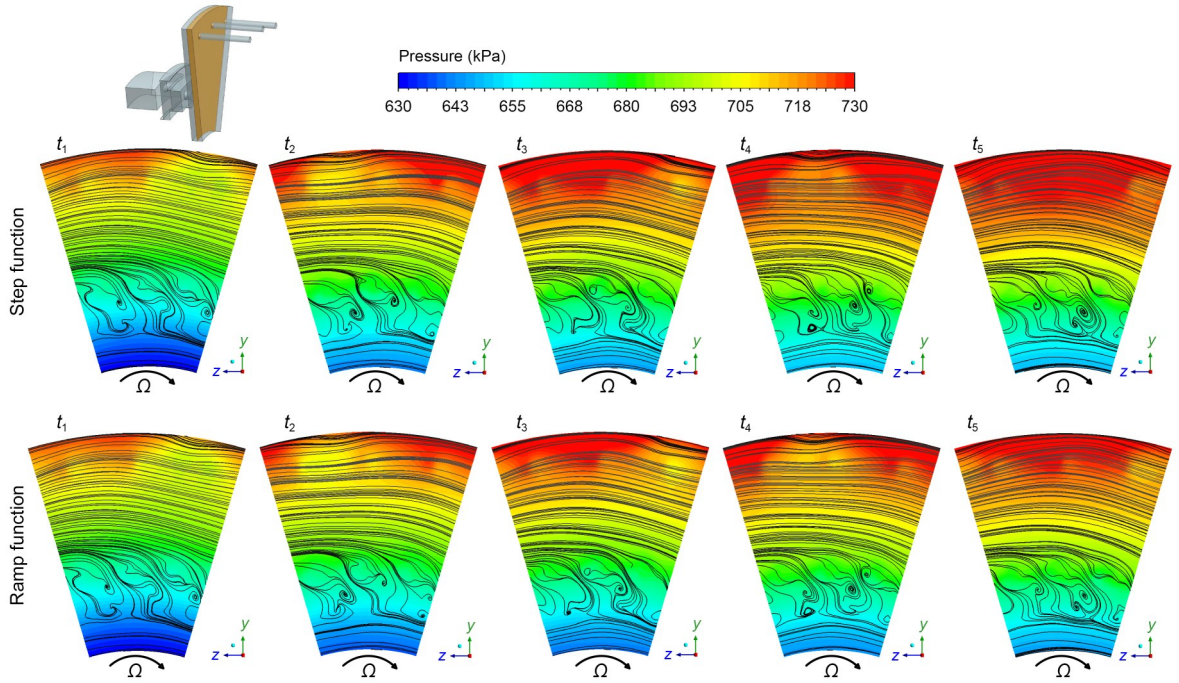


**Fig. 13 Distribution of instantaneous pressure field and streamline on the mid-section plane in the co-rotating cavity**

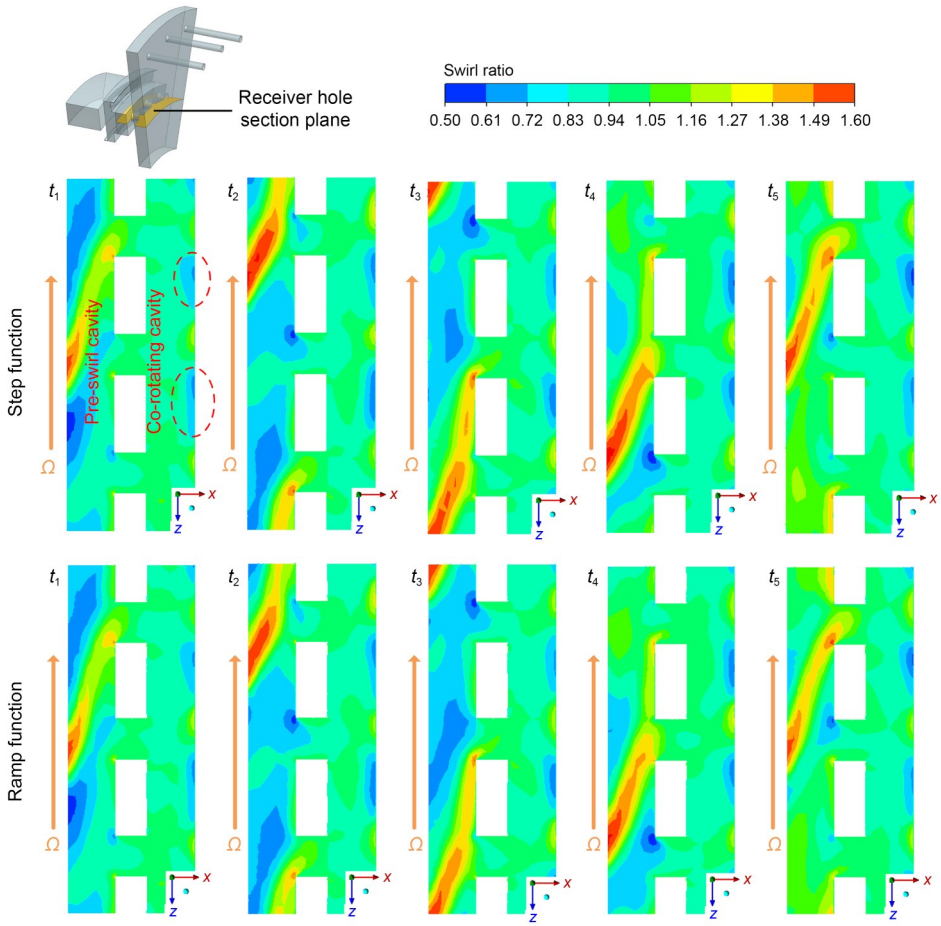


**Fig. 14 Instantaneous swirl-ratio distribution in the receiver hole**

progressed, the high-value region swept through three receiver holes sequentially. In the receiver holes and cover-plate cavity, the swirl ratio was relatively uniform, approximately $\beta$=1.0. Near the downstream wall of the cover-plate cavity, the swirl ratio was relatively low because the gas in these regions was less accelerated by the incoming gas from the receiver holes. For both step and ramp functions, the distributions of the swirl ratio in the receiver holes were similar, and the changes with time followed the same rule.

### 4.2 Cases III and IV: the effect of different intake-pressure pulsation frequencies

In the pre-swirl system, the oscillation of flow parameters induced by the bulk-cavity effect and the air-inertia force can be simplified as a sine function or fitted by one (Mao et al., 2019). For Cases III and IV, we defined different-frequency sine functions with the same amplitude to simulate periodic pulsation in the pre-swirl system.

When the pre-swirl inlet-pressure fluctuation is modeled as a sine function, the flow parameters in the system will fluctuate around stable values without reaching a steady state. To simplify the analysis of the transient process when using a sine function, we averaged parameters within a period, treating the average values as stable under these conditions. In this section, we focus on two key parameters: the air-supply flow rate and the temperature drop of the pre-swirl system. The responses of mass flow and temperature drop are presented in Figs. 15 and 16, respectively. To mitigate the influence of flow-field inertia in the initial period, we intercepted the curve distribution of the intermediate period and applied a phase shift. As depicted in Fig. 15, the mass flow exhibited sinusoidal changes. Due to the rotation effect, the sine curve was also superimposed with a high-frequency pulsation signal. With an increase in the inlet-pressure change frequency, the stable value of mass flow $\Delta m$ remained approximately constant, hovering around $m_6/m_7$=4.58. The maximum

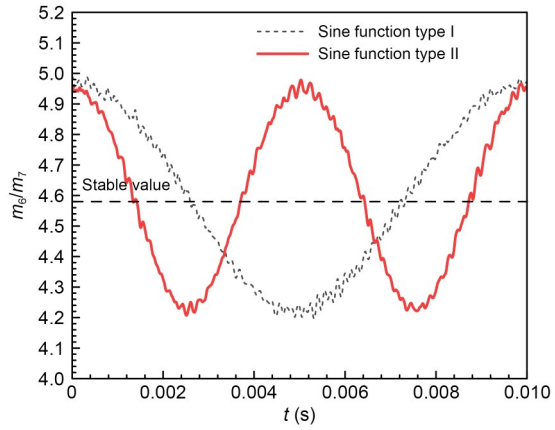


**Fig. 15 Response of mass flow rate at outlet of the supply hole**

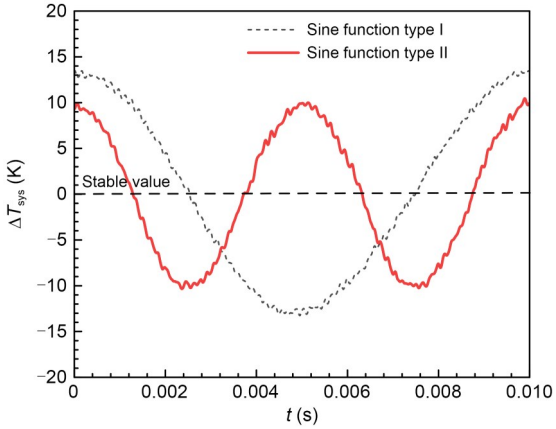


**Fig. 16 Actual temperature-drop response**

deviations of mass flow also varied little with frequency. This is because as the frequency increased, although the time for acceleration and deceleration of the fluid within one cycle decreased, the slope of pressure variations at the inlet increased. This led to a greater slope for fluid acceleration and deceleration, ultimately resulting in a smaller difference in the maximum deviation of mass flow rate variation at the outlet of the supply hole. In Fig. 16, one can see that as the frequency increased from 100 Hz to 200 Hz, the maximum deviations for $\Delta T_{sys}$ changed from around ±13 K to ±10 K. This is because when the inlet pressure exhibited periodic variations, the downstream fluid in the pre-swirl system periodically compressed and expanded. When the frequency of the inlet-pressure pulsations decreased, the time for compression and expansion within one cycle increased, leading to a greater amplitude of change in the relative total temperature of the downstream gas. Therefore, low-frequency pressure pulsations have a significant impact on the air-supply quality of turbine blades. However, they have little effect on the stable value of $\Delta T_{sys}$. For sine function types I and II, the stable values of $\Delta T_{sys}$ remain around 0 K.

To better understand the influence of sine function frequency on temperature, we conducted a detailed analysis of the relative total temperature $T^*_{rel}$ distribution in the cover-plate cavity over a specific time period. Fig. 17 illustrates the instantaneous relative total temperature distribution within the cover-plate cavity. In the region near radius $r_1$, the relative total temperature $T^*_{rel}$ was low. As the local radius $r$ exceeded $r_1$ and increased, $T^*_{rel}$ also increased. In the high-radius region, $T^*_{rel}$ reached the highest point, a phenomenon that will be further demonstrated in Fig. 19. At different times in a period ($t_{period}$), the $T^*_{rel}$ distribution in the cover-plate cavity showed periodic variation. The distributions of relative total temperature are noticeably different for sine function types I and II. It is evident that the $T^*_{rel}$ for sine function type I in the high-radius region is slightly higher than that at time $t/t_{period}$=0.2. This periodic relative total temperature change also influenced the temperature drop of the pre-swirl system accordingly.

The swirl-ratio distribution on the section of the cover-plate cavity is illustrated in Fig. 18. The gas

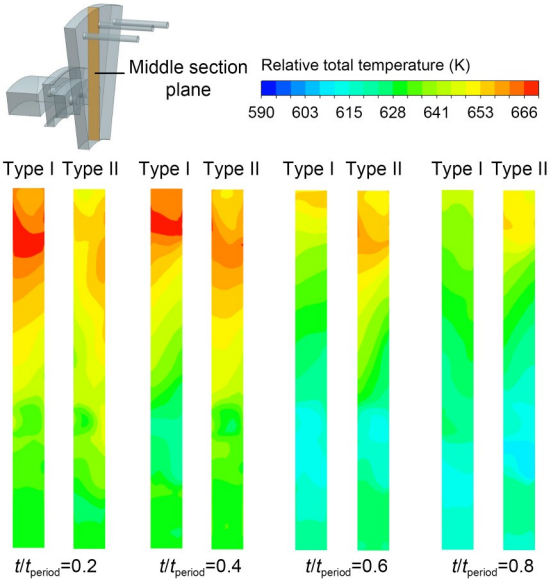


**Fig. 17 Effect of pressure frequency on instantaneous relative total temperature distribution in the cover-plate cavity. Yellow in the schematic diagram indicates the middle section plane. $t_{period}$ denotes a period, with a duration of 0.01 s for sine function type I and 0.005 s for sine function type II. References to color refer to the online version of this figure**

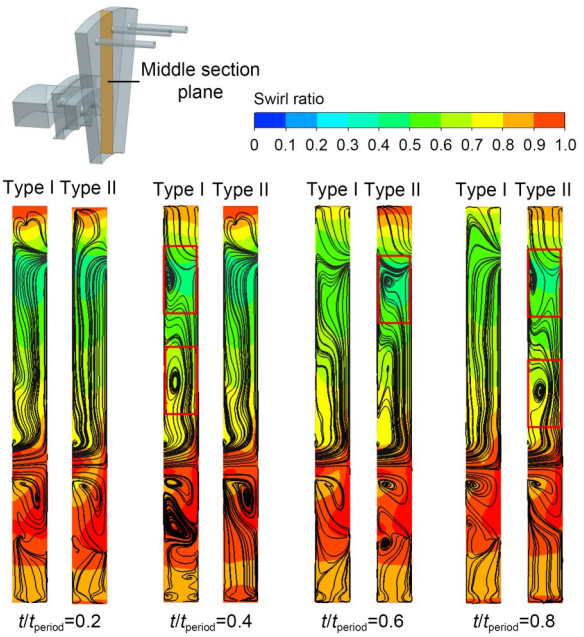


**Fig. 18 Effect of pressure frequency on instantaneous swirl-ratio and streamline distribution in the cover-plate cavity**

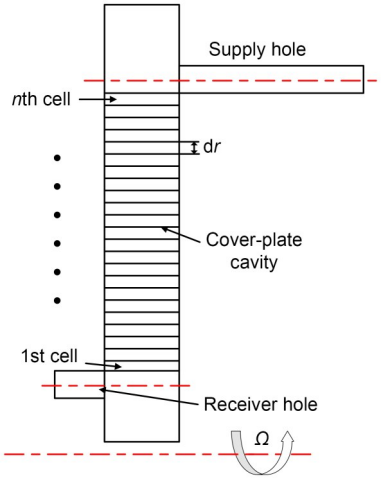


**Fig. 19 Schematic diagram of cells in the cover-plate cavity**

entered the cover-plate cavity and first impacted the rear wall. Due to the combined influence of the upstream pre-swirl nozzle and receiver-hole walls, the swirl ratio in the cover-plate cavity reached its highest value behind the receiver holes, around $\beta$=1.0. The fluid entering the cavity was divided into upper and lower streams, and migrated to the high and low radii, respectively. The process of gas migration to the high radius satisfied the conservation of angular momentum, while due to the mixing loss, the gas swirl ratio decreased. As the frequency increased, the flow-field structure in the cavity became more complex, undergoing more intense changes. The generation-dissipation process of the vortex system at the middle and high radii can be clearly observed for sine function types I and II.

The temperature distribution along the cover-plate cavity radial direction can be calculated as follows (Shen and Wang, 2022). As shown in Fig. 19, the cover-plate cavity was divided into several cells, with thickness d$r$. The temperature rise $\Delta T$ in a single small cell is:

$$\Delta T=\frac{q_{\mathrm{w}}\times\pi\left[(r+\mathrm{d}r)^2-r^2\right]}{mC_{\mathrm{p}}}+\omega_{\mathrm{a}}^2\frac{\left[(\beta_{\mathrm{r}}-1)r\right]^2-\left[(\beta_{\mathrm{r}+\mathrm{d}r}-1)(r+\mathrm{d}r)\right]^2+(r+\mathrm{d}r)^2-r^2}{2C_{\mathrm{p}}},\tag{19}$$

where $q_{\mathrm{w}}$ is the wall heat flux. The cavity wall is assumed here to be adiabatic. Eq. (19) can be simplified as:

$$\Delta T=\omega_{\mathrm{a}}^2\frac{\left[(\beta_{\mathrm{r}}-1)r\right]^2-\left[(\beta_{\mathrm{r}+\mathrm{d}r}-1)(r+\mathrm{d}r)\right]^2+(r+\mathrm{d}r)^2-r^2}{2C_{\mathrm{p}}}.\tag{20}$$

We conducted a qualitative analysis based on Eq. (20) to explore the relationship between the temperature distribution along the radial direction of the cover-plate cavity, the swirl-ratio distribution (shown in Fig. 18), and the temperature near the receiver hole (shown in Fig. 17). In Fig. 18, it is evident that swirl-ratio distribution along the radial direction remained similar with different frequencies at the same time. The temperature distribution was primarily influenced by the upstream temperature, as indicated by Eq. (20). Observing Fig. 17, we note that the temperature near the receiver hole changed periodically under the influence of upstream pressure disturbance. This periodic change resulted in fluctuations throughout the cover-plate cavity.

## 5 Conclusions

In this study, we looked at a cover-plate pre-swirl system for an aero engine, using a real engine structure

with three cavities and seal inlet/outlet structures. The transient responses of thermal and aerodynamic characteristics were investigated numerically by means of unsteady 3D Reynolds-averaged Navier-Stokes equations coupled with the SST $k$-$\omega$ turbulence model. Our aim was to determine the effect of different inlet aerodynamic conditions for the step inlet, ramp inlet, and sinusoidal inlet. The chosen real engine structure is similar to the structure studied in the literature (Liu et al., 2018, 2021). The results indicate that, among various parameters, the actual temperature drop exhibits a noticeable overshoot phenomenon. Additionally, the influence of low-frequency inlet-flow fluctuation on the quality of blade air supply is more obvious than that of high frequency. The important conclusions are summarized as follows:

(1) Due to fluctuation at the pre-system inlet and outlet, the retention mass flow in the system undergoes oscillation before stabilizing at a steady value. The mass flow response at the supply-hole outlet is characterized by two distinct periods: a fast-increase period and a slow-increase period. The fast-increase period is shorter for the step function than for the ramp function. Notably, no obvious mass flow overshoot occurs either at the supply-hole outlet or the seal outlet.

(2) With the same intake functions (step and ramp), a lag phenomenon is observable in the response of volume-average parameters. When considering these two intake functions, the growth rates of volume-average parameters vary. In the following quasi-steady-state process, it becomes essential to consider the influence of nonlinear growth. For a 10% jump in inlet pressure, the dimensionless jump amplitude $I$ of $\rho_{ave}$ is calculated to be 4.21%, and the dimensionless jump amplitude $I$ of $p^*_{rel}$ is $I$=3.77%.

(3) Due to compression effects caused by macroscopic mass-transport fluctuations, the actual temperature drop in the cover-plate pre-swirl system exhibits a noticeable overshoot phenomenon. The calculated overshoot value $\sigma$ for the step function is 460%, which is higher than for the ramp function ($\sigma$=220%). Additionally, the peak time $t_p$ for the step function is 75% shorter than for the ramp function.

(4) For different intake-pressure pulsation frequencies, temperature drop and response of mass flow at the supply-hole outlet are significantly influenced. However, the pressure fluctuation has little effect on the stable values of mass flow and temperature drop. Due to the varying intake-pressure pulsation frequencies, the durations of gas compression and expansion within a period also differ. This results in a more obvious influence of low-frequency pulsation on the maximum deviation of $\Delta T_{sys}$, potentially affecting the air-supply quality of the turbine blades.

In future studies, we intend to look in detail at the influence of angular velocity change in the boundary condition on a pre-swirl system. In addition, we will consider the heat transfer between the cover-plate cavity and the turbine disk, so as to better implement a simulation under actual operating conditions.

## Acknowledgments

This work is supported by the Strategic Priority Research Program of the Chinese Academy of Sciences (No. XDC0160000), the National Natural Science Foundation of China (No. 52122603), the Excellence Research Group Program (No. 52488101), the Shandong Provincial Natural Science Foundation of China (No. ZR2024JQ011), the Project of National Key Laboratory of Science and Technology on Advanced Light-duty Gas-turbine (No. 2023-JJ-Y04), the National Science and Technology Major Project of China (No. J2019-III-0003-0046), and the Taishan Scholars Program of China. The authors wish to thank Prof. Songling LIU (Northwestern Polytechnical University, China) for his instructive comments and suggestions, and Beijing Super Cloud Computing Center, China for the cloud computing support.

## Author contributions

Qiang DU designed the research. Zengyan LIAN and Guang LIU processed the corresponding data. Yifu LUO wrote the first draft of the manuscript. Lei XIE helped to organize the manuscript. Qingzong XU revised and edited the final version.

## Conflict of interest

Yifu LUO, Qiang DU, Zengyan LIAN, Guang LIU, Lei XIE, and Qingzong XU declare that they have no conflict of interest.

## References

Benim AC, Brillert D, Cagan M, 2004. Investigation into the computational analysis of direct-transfer pre-swirl systems for gas turbine cooling. ASME Turbo Expo: Power for Land, Sea, and Air, p.453-460. https://doi.org/10.1115/GT2004-54151

Blazek J, 2015. Computational Fluid Dynamics: Principles and Applications. 3rd Edition. Elsevier, Amsterdam, the Netherlands.

Bonfiglioli A, Paciorri R, 2014. Convergence analysis of shock-capturing and shock-fitting solutions on unstructured grids. *AIAA Journal*, 52(7):1404-1416. https://doi.org/10.2514/1.J052567

Ciampoli F, Hills NJ, Chew JW, et al., 2008. Unsteady numerical simulation of the flow in a direct transfer pre-swirl system. ASME Turbo Expo: Power for Land, Sea, and Air, p.1647-1655. https://doi.org/10.1115/GT2008-51198

Courant R, Friedrichs K, Lewy H, 1928. Über die partiellen differenzengleichungen der mathematischen physik. *Mathematische Annalen*, 100(1):32-74 (in German). https://doi.org/10.1007/BF01448839

Ding ST, Wang ZY, Qiu T, et al., 2018. Probabilistic failure risk assessment for aeroengine disks considering a transient process. *Aerospace Science and Technology*, 78:696-707. https://doi.org/10.1016/j.ast.2018.05.017

Dittmann M, Geis T, Schramm V, et al., 2002. Discharge coefficients of a preswirl system in secondary air systems. *Journal of Turbomachinery*, 124(1):119-124. https://doi.org/10.1115/1.1413474

Dutton JC, Coverdill RE, 1997. Experiments to study the gaseous discharge and filling of vessels. *The International Journal of Engineering Education*, 13(2):123-134.

Gallar L, Calcagni C, Llorens C, et al., 2011. Time accurate modelling of the secondary air system response to rapid transients. *Proceedings of the Institution of Mechanical Engineers, Part G: Journal of Aerospace Engineering*, 225(8):946-958. https://doi.org/10.1177/0954410011398280

Gan CY, Ding ST, Qiu T, et al., 2024. Model-based safety analysis with time resolution (MBSA-TR) method for complex aerothermal–mechanical systems of aero-engines. *Reliability Engineering & System Safety*, 243:109864. https://doi.org/10.1016/j.ress.2023.109864

Gong WB, Liu GW, Wang JY, et al., 2022. Aerodynamic and thermodynamic analysis of an aero-engine pre-swirl system based on structure design and performance improvement. *Aerospace Science and Technology*, 123:107466. https://doi.org/10.1016/j.ast.2022.107466

Karabay H, Chen JX, Pilbrow R, et al., 1999. Flow in a "cover-plate" preswirl rotor–stator system. *Journal of Turbomachinery*, 121(1):160-166. https://doi.org/10.1115/1.2841225

Karabay H, Wilson M, Owen JM, 2001. Predictions of effect of swirl on flow and heat transfer in a rotating cavity. *International Journal of Heat and Fluid Flow*, 22(2):143-155. https://doi.org/10.1016/S0142-727X(00)00076-X

Karnahl J, von Wolfersdorf J, Tham KM, et al., 2012. Computational fluid dynamics simulations of flow and heat transfer in a preswirl system: influence of rotating-stationary domain interface. *Journal of Engineering for Gas Turbines and Power*, 134(5):052502. https://doi.org/10.1115/1.4004730

Kim S, Lee J, Kim D, et al., 2022. Effect of fillet radius of receiver hole on the performance of gas turbine pre-swirl system. *Journal of Mechanical Science and Technology*, 36(12):6073-6081. https://doi.org/10.1007/s12206-022-1122-6

Lee J, Lee H, Park H, et al., 2021. Design optimization of a vane type pre-swirl nozzle. *Engineering Applications of Computational Fluid Mechanics*, 15(1):164-179. https://doi.org/10.1080/19942060.2020.1847199

Liao GH, Wang XJ, Li J, 2014. Numerical investigation of the pre-swirl rotor–stator system of the first stage in gas turbine. *Applied Thermal Engineering*, 73(1):940-952. https://doi.org/10.1016/j.applthermaleng.2014.08.054

Lin AQ, Liu GW, Yu XX, et al., 2022. Comprehensive investigations on fluid flow and heat transfer characteristics of a high-speed rotating turbine disk cavity system of aero-engine. *International Communications in Heat and Mass Transfer*, 136:106170. https://doi.org/10.1016/j.icheatmasstransfer.2022.106170

Liu GW, Liu YX, Kong XZ, et al., 2017. A new design of vane-shaped hole pre-swirl nozzle. *Proceedings of the Institution of Mechanical Engineers, Part A: Journal of Power and Energy*, 231(1):14-24. https://doi.org/10.1177/0957650916673462

Liu YX, Liu GW, Kong XZ, et al, 2018. Experimental testing and numerical analysis on the nozzle effects in preswirl system. *Journal of Propulsion and Power*, 34(4):1015-1025. https://doi.org/10.2514/1.B36700

Liu YX, Yue BZ, Kong XZ, et al., 2021. Design and performance analysis of a vane shaped rotating receiver hole in high radius pre-swirl systems for gas turbine cooling. *Aerospace Science and Technology*, 115:106807. https://doi.org/10.1016/j.ast.2021.106807

Liu YX, Lu BY, Kong XZ, et al., 2023. Effects of the misalignment and axial gap on performance of a cover-plate pre-swirl system with impellers for gas turbine cooling. *Physics of Fluids*, 35(10):105110. https://doi.org/10.1063/5.0166382

Mao SS, Wang SF, Hu WX, 2019. Study on transient response characteristics of rotor-stator cavity with typical intake function. *Journal of Propulsion Technology*, 40(1):175-183 (in Chinese). https://doi.org/10.13675/j.cnki.tjjs.180032

Menter FR, 1994. Two-equation eddy-viscosity turbulence models for engineering applications. *AIAA Journal*, 32(8):1598-1605. https://doi.org/10.2514/3.12149

Nicholas TEW, Pernak MJ, Scobie JA, et al., 2023. Transient heat transfer and temperatures in closed compressor rotors. *Applied Thermal Engineering*, 230:120759. https://doi.org/10.1016/j.applthermaleng.2023.120759

Nikolaidis T, Wang HN, Laskaridis P, 2020. Transient modelling and simulation of gas turbine secondary air system. *Applied Thermal Engineering*, 170:115038. https://doi.org/10.1016/j.applthermaleng.2020.115038

Owen JM, Pincombe JR, Rogers RH, 1985. Source–sink flow inside a rotating cylindrical cavity. *Journal of Fluid Mechanics*, 155:233-265. https://doi.org/10.1017/S0022112085001793

Popp O, Zimmermann H, Kutz J, 1998. CFD analysis of cover-plate receiver flow. *Journal of Turbomachinery*, 120(1):43-49. https://doi.org/10.1115/1.2841386

Roache PJ, 1998. Verification of codes and calculations. *AIAA Journal*, 36(5):696-702.

https://doi.org/10.2514/2.457

Roy CJ, McWherter-Payne MA, Oberkampf WL, 2003. Verification and validation for laminar hypersonic flowfields, part 1: verification. *AIAA Journal*, 41(10):1934-1943. https://doi.org/10.2514/2.1909

Shen WJ, Wang SF, 2022. Large eddy simulation of turbulent flow and heat transfer in a turbine disc cavity with impellers. *International Communications in Heat and Mass Transfer*, 139:106463. https://doi.org/10.1016/j.icheatmasstransfer.2022.106463

Thomas JL, Diskin B, Rumsey CL, 2008. Towards verification of unstructured-grid solvers. *AIAA Journal*, 46(12): 3070-3079. https://doi.org/10.2514/1.36655

Wilcox DC, 1988. Reassessment of the scale-determining equation for advanced turbulence models. *AIAA Journal*, 26(11): 1299-1310. https://doi.org/10.2514/3.10041

Zhang K, Naguib AM, 2011. Effect of finite cavity width on flow oscillation in a low-Mach-number cavity flow. *Experiments in Fluids*, 51(5):1209-1229. https://doi.org/10.1007/s00348-011-1142-y

Zimmermann H, 1990. Some aerodynamic aspects of engine secondary air systems. *Journal of Engineering for Gas Turbines and Power*, 112(2):223-228. https://doi.org/10.1115/1.2906166